Check for updates

The fabrication of TiO$_2$-supported clinoptilolite *via* F$^-$ contained hydrothermal etching and a resultant highly energetic {001} facet for the enhancement of its photocatalytic activity†

Anadil Gul,‡ Raza Ullah,‡ Jihong Sun, [ID]* Tallat Munir and Shiyang Bai*

TiO$_2$-supported clinoptilolite (TiO$_2$/CP) was synthesized in the presence of F$^-$ ions. Various characterizations demonstrated that the particle size of loaded TiO$_2$ increased linearly with an increase in the temperature and concentration of F$^-$ ions. In particular, the additive F$^-$ ions were favored to produce the mutually independent co-exposed {001} and {101} facets of loaded TiO$_2$, while TiO$_2$/CPs synthesized in the absence of F$^-$ ions were dominated by the thermodynamically stable {101} facet. As photocatalysts for the removal of crystal violet or methyl orange dyes under UV-irradiation in aqueous solutions, TiO$_2$/CPs (ACP6) synthesized in the presence of F$^-$ ions significantly improved the degradation efficiency, as compared to ACP3 obtained in the absence of F$^-$ ions. These results elucidated that the highly energetic {001} exposed facet, large particle size and fine dispersion of loaded TiO$_2$ in TiO$_2$/CP accounts for its best photocatalytic performance. The effected mechanism of operational parameters on the degradation performances is proposed.

1. Introduction

With the increasing demands of energy- and environment-related problems, photocatalysis, as a light-driven photochemical process over the surface of a photocatalyst, has attracted increasing attention over the last few decades due to its potential applications in the fields of wastewater treatment and the generation of renewable energy.[1,2] Although TiO$_2$-based photocatalysis has been over-exploited in the past few decades, there are still some challenges related to the reaction efficiency, complicated treatment of catalyst recovery step, electron–hole recombination rate and electron–hole transport mechanism of TiO$_2$, which restrain the large-scale practical application of the process.[3–5] To achieve higher efficiency in the practical application of TiO$_2$, the tailoring of its physical properties, such as phase composition, exposed crystal facets, average particle size, surface area, crystallinity and porosity, are of key importance.[6–9] The immobilization of TiO$_2$ onto the surface of some suitable support is an encouraging alternative to the inherent limitations of unsupported TiO$_2$.

The preparation of the TiO$_2$/zeolite composite photocatalyst has attracted increasing attention over recent years, as the composite configuration tailors the photocatalytic properties of loaded TiO$_2$ by controlling the particle size, bandgap, surface area, loading content and porosity of loaded TiO$_2$. Moreover, the physical and electronic properties of the composite photocatalysts can be regulated by interfacial interactions between TiO$_2$ and zeolite. The use of zeolite as a supporting matrix for TiO$_2$ nanoparticles has also been found to enhance the adsorption capacity[10] and dispersion of titania,[11] which in turn improve the photoactivity of the system. Generally, the immobilization of TiO$_2$ onto the surface of zeolite can be achieved by numerous methods including sol–gel,[10] hydrothermal,[12] impregnation,[11] and solid-state dispersion methods.[13] Among the aforementioned methods, the hydrothermal method is an effective route for immobilizing TiO$_2$ onto the surface of zeolite with high surface area, good crystallinity and variant particle size,[14] which offer several advantages such as the formation of the anatase phase at relatively low temperature, low agglomeration between particles, defect-free nano-crystals with high surface area, and narrow particle size distribution.[15,16]

Clinoptilolite (CP), being one of the most abundantly occurring zeolites in nature, is regarded as the best candidate as a support for TiO$_2$.[17–19] Though significant research is available on the synthesis and application of TiO$_2$/CP composites, the literature still lacks data relating to the loading of anatase TiO$_2$ onto CP with controlled particle size and highly reactive exposed crystal facets. Recently, intensive research interest has been focused on controlling the crystal particle size and exposed facets of TiO$_2$ to enhance its photocatalytic

Beijing Key Laboratory for Green Catalysis and Separation, Department of Environmental and Chemical Engineering, Beijing University of Technology, Beijing 100124, P. R. China. E-mail: jhsun@bjut.edu.cn; sybai@bjut.edu.cn

‡ Equal contribution.

performance.[20,21] There exists an optimum particle size for excellent photocatalytic performance of TiO_2 due to the competing effects of the effective particle size on light absorption and scattering efficiency. Almquist and Biswas[22] synthesized anatase TiO_2 particles in the range of 5 to 165 nm and found that an optimum particle size of 25 to 40 nm exhibited excellent photoactivity. The tailoring of anatase TiO_2 crystals with the termination of specific facets has received great interest for many years. As reported by Liu *et al.*,[9] the anatase phase {001} facet was found to be the most reactive with an average surface energy of 0.90 J mol^{-2}; therefore, the photocatalytic performance of anatase TiO_2 depends not only on its particle size, but also on the type of exposed crystal facets. However, unfortunately, most available anatase TiO_2 is dominated by the thermodynamically stable {101} facet during the crystallization process due to its relatively low surface energy, *i.e.* 0.44 J mol^{-2}.[23] The breakthrough in controlling the synthesis of crystals with a high percentage of reactive high energy {001} facets was not made until 2008.[24] Roy *et al.*[25] demonstrated that among the various facets, {101} was the least active towards methyl orange (MO) degradation, whilst an optimum {001}/{101} ratio resulted in excellent performance because of the reduced electron–hole recombination rate. In order to enhance the photocatalytic performance of TiO_2, a large group of researchers are making efforts to synthesize anatase TiO_2 with highly reactive exposed facets, *i.e.* {001}. Hence, TiO_2/CPs with highly reactive exposed facets *i.e.* {001} are still highly desired and pursued in the field of heterogeneous photocatalysis. Numerous methods have been developed to fabricate anatase TiO_2 nanocrystals with {001} exposed facets, in which surface fluorination is the most effective in stabilizing {001} facets based on first-principles calculations.[23,24]

Herein, TiO_2/CP photocatalysts with controlled anatase TiO_2 particle size and exposed highly reactive crystal facets were synthesized under different hydrothermal treatment temperatures and concentrations of fluoride ions (F^- ions) in an aqueous solution of $TiCl_4$. The effect of hydrothermal treatment temperature and additive amount of F^- ions on the photocatalytic activity of TiO_2/CP was investigated in detail *via* the degradation of crystal violet (CV) and methyl orange (MO) dyes under UV-irradiation in aqueous media. F^- ions were used as tailoring agents to expose the highly energetic {001} facet of the loaded TiO_2 in order to enhance its photocatalytic activity. The as-prepared TiO_2/CP catalysts were characterized *via* X-ray diffraction (XRD), scanning electron microscopy (SEM), transmission electron microscopy (TEM), inductively coupled plasma-optical emission spectrometry (ICP-OES), X-ray Photoelectron Spectroscopy (XPS), Fourier Transform Infrared (FT-IR), UV-visible spectroscopy and BET-isotherm. Finally, the degradation kinetics of CV and MO dye in the aqueous solutions were elucidated.

2. Experimental

2.1. Materials

Natural CP with a Si/Al ratio of 10.63 was supplied by Guo-TouShengShi Science and Technology Co. Ltd. $TiCl_4$ (99% purity), NH_4F (96.0%), CV dye (high purity biological stain), and MO dye were obtained from J & K Co. Ltd. All solutions were made in deionized water with a resistivity of 18.25 MΩ cm.

2.2. Synthesis of TiO_2/CP catalysts

The finely divided powdered natural CP was first purified by heating its suspension in deionized water (10 g L^{-1}) at 70 °C under continuous vigorous stirring for 8 hours. The resulting suspension was then allowed to settle down prior to filtration and then washed thoroughly with deionized water. TiO_2/CP photocatalysts were synthesized using a procedure similar to that reported by Ullah *et al.*[14] In a typical procedure, 1.00 g of CP was dispersed in 25 mL of 0.25 M $TiCl_4$ solution made in ice-cold water and the suspension was then autoclaved on oil baths under continuous vigorous stirring for 5 hours at 100, 150, and 200 °C. The precipitate was then separated by filtration, washed thoroughly with deionized water and dried in an oven at 80 °C overnight. The obtained products were ground to a fine powder and named ACP1, ACP2, and ACP3, corresponding to the hydrothermal temperature at 100, 150, and 200 °C, respectively.

Keeping the other conditions constant as used for the first set of three catalysts, the second set of four catalysts were synthesized at 200 °C by adding 0.08, 0.15, 0.25, and 0.35 M NH_4F to 0.25 M $TiCl_4$ solution, and named ACP4, ACP5, ACP6, and ACP7, respectively. Pure TiO_2 was also made by the same procedure using 0.25 M F^- ions without adding CP.

A representative scheme showing the preparation procedures and the structure of TiO_2/CPs is illustrated in Fig. S1 of the ESI† section.

2.3. Characterizations

The phase compositions and crystalline structures of the TiO_2/CP catalysts were analyzed by X-ray diffractometer (Beijing Purkinje General Instrument Co. Ltd), having a CuKα irradiation source, and 2θ (diffraction angle) ranging from 5–75°. The supported TiO_2, crystallite size was calculated with the help of Scherrer's equation ($D = k\lambda/\beta \cos \theta$), where D is the estimated crystallite size (nm), k is a constant (0.9), λ is the X-ray wavelength (0.15432 nm), β is the peak width at half of the maximum height, θ is the diffraction angle. ICP-OES (Perkin Elmer Optima 2000-DV) was used to analyze the elemental composition and weight % of TiO_2 in the synthesized samples (TiO_2/CP). The chemical structures of the samples were examined *via* FT-IR spectrophotometer in the range of 400–4000 cm^{-1}. N_2 adsorption–desorption isotherms were used to determine the specific surface area of synthesized samples at −196 °C, with the help of a JW-BK300 (Beijing Sci. & Techno. Co. Ltd). The samples were degassed at 120 °C for 6 hours prior to each measurement in order to remove all the adsorbed gas molecules in the samples. The structural morphology and particle size of the synthesized samples (TiO_2/CP) were examined using scanning and transmission electron microscopy (JEOLJEM-200 and JEOL-2010, respectively). The operating voltage was 15.0 kV for SEM and 200 kV for TEM. The optical bandgaps of the samples were determined using a Shimadzu UV-2600 spectrophotometer. The

pH$_{pzc}$ (point of zero charge) was measured with the help of a Zeta-sizer (Malvern Instrument Ltd, UK) through light scattering at different pH values. Surface chemical analysis of the synthesized samples (TiO$_2$/CP) was performed by XPS spectra (ESCALAB 250Xi, Germany). The total organic carbon (TOC) removal efficiencies of CV and MO dye *via* photocatalytic degradation were investigated *via* vario TOC (UK).

2.4. Photocatalytic degradation experiments

The photocatalytic evaluation of the obtained TiO$_2$/CPs for the degradation of CV and MO dyes was carried out in a 250 mL glass beaker containing 100 mL aqueous solution at room temperature. A set of three 20 W high-pressure UVC Hg lamps enclosed in a rectangular steel box, was used as the irradiation source. Before being subjected to the UV-light source, the reaction mixture was stirred for 30 min continuously in the dark to reach the adsorption–desorption equilibrium. The amount of both the dyes adsorbed was less than 5% for all the photocatalysts synthesized, which indicates that adsorption has a negligible role in the removal process. Therefore, the degradation process was mainly focused in the removal of these dyes from the reaction mixture. At a set time, the aliquots of used samples were withdrawn, centrifuged prior to the analysis to remove the suspended catalyst particles and then analyzed using a UV-vis spectrophotometer. Each experiment was carried out in duplicate in order to validate the results.

The following eqn (1) was used for the percentage degradation (X%) calculation of CV and MO dyes, as follows:

$$X\% = (C_0 - C_e) \cdot \frac{100}{C_0} \tag{1}$$

where C_0 and C_e are the initial and final concentrations (mM) of the dye at equilibrium.

The TOC removal percentage (%) was estimated using the following expression (2):

$$\text{TOC removal percentage } (\%) = \left(1 - \frac{\text{TOC}}{\text{TOC}_0}\right) \times 100\% \tag{2}$$

where TOC corresponds to time t, and TOC$_0$ corresponds to the initial conditions.

3. Results and discussion

3.1. Characterization of TiO$_2$/CPs

The XRD patterns of parent natural CP, TiO$_2$, and TiO$_2$/CPs (ACP1, ACP3, ACP4, and ACP6) are shown in Fig. 1. The heulandite (HEU) structure of CP and the crystal phase of TiO$_2$ were confirmed by comparison with the Joint Committee on Powder Diffraction Standards (JCPDSs), in which, the characteristic diffraction peaks at 2θ values of 9.98, 11.27, 22.29, 26.82, 30.07, and 32.23° belonged to the major components of the CP (as shown in Fig. 1a), and those at 25.5, 38.2, 48.3, 54.2, 55.4, and 62.5° corresponded to anatase phase TiO$_2$ (as shown in Fig. 1f), which are indexed as (101), (001), (200), (105), (211), and (204) crystal planes, respectively. With the improved hydrothermal temperatures from 100 °C for ACP1 (Fig. 1b) to 200 °C for ACP3 (Fig. 1c), or increased concentrations of used F$^-$ ions
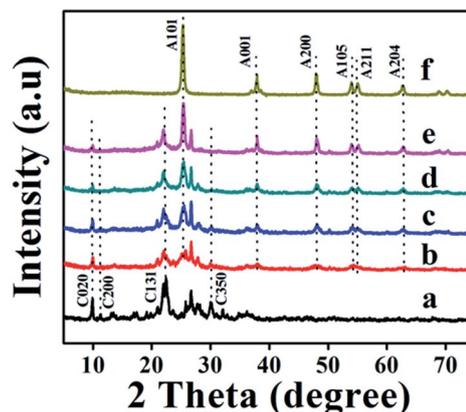

Fig. 1 XRD patterns of (a) natural CP, (b) ACP1, (c) ACP3, (d) ACP4, (e) ACP6, and (f) pure TiO$_2$.

form 0.08 M for ACP4 (Fig. 1d) to 0.25 M for ACP6 (Fig. 1e), the decline in peak intensity of CP characteristic phases, but the enhancement in the intensity of anatase peaks may be because TiO$_2$ particles effectively covered the surfaces of CP during composite formation and hindered peaks of CP from being detected by XRD patterns. Another reason may be related to the etching effect of used F$^-$ ions at a high hydrothermal temperature on the excessive dealumination of CP structures.[26] Furthermore, the crystallite size of loaded TiO$_2$ calculated using Scherrer's equation, as shown in Table 1, presented the increasing tendency from 7.8 to 17.7 nm along with enhancements of temperature and concentrations of used F$^-$ ions. As can be seen in Fig. 1, the intensity of the (004) diffraction peak, being used (I_{004}/I_{101}) to represent the highly energetic {001} facet in TiO$_2$/CP,[9] remarkably improved with enhancements of temperature and concentrations of used F$^-$ ions, and was also higher than that of pure anatase TiO$_2$ (*ca.* 0.30, as shown in Table S1 of the ESI† section, corresponding to the reference standard (JCPDS. 21-1272) which presented I_{004}/I_{101} of (0.2)[9]). These observations suggest the preferential orientation growth along the {001} facet direction for TiO$_2$/CPs (ACP4-ACP7); in other words, the existence of both F$^-$ ions and CPs plays a significant role in exposing the highly energetic {001} facet of loaded TiO$_2$. However, in the absence of CP, the hydrothermal treatment of the TiO$_2$ precursor in HF solution easily leads to the formation of pure anatase particles with a relatively low intensity of {004} diffraction peaks (as seen from the I_{004}/I_{101} values in Table S1 of the ESI† section). This unique co-existence of highly energetic {001} and thermodynamically stable {101} facets in TiO$_2$/CP (ACP6) is responsible for the synergistic removal of CV and MO dyes from aqueous solution under UV-irradiation.

All the TiO$_2$/CP samples formed in the presence of F$^-$ ions exhibited much sharper and higher characteristic peaks of loaded TiO$_2$, which may be ascribed to their highly crystalline characteristics. Table S1† also shows that the crystallinity degrees of CP support decreased, while that of loaded TiO$_2$ increased along with the enhancement of the temperature and concentration of F$^-$ ions during hydrothermal treatments. The

Table 1 Collections of various parameters of CP and TiO_2/CPs

| Sample | Formula | TiO_2 amount[a] (wt%) | TiO_2 phase | TiO_2 particle size (nm) | | Si/Al[d] (molar ratio) | S_{BET}[e] (m² g⁻¹) | Bandgap (eV) | |
				XRD[b]	SEM[c]			$n = 2$	$n = 1/2$
CP	$Na_{0.75}K_{1.89}Al_{8.06}Si_{85.70}O_{184.81}$	—	—	—	—	10.63	15.8	—	—
ACP1	$Ti_{21.57}Na_{1.36}K_{1.23}Al_{6.12}Si_{88.24}O_{230.10}$	27.31	Anatase	7.80	4.7	14.41	193.7	2.73	3.33
ACP2	$Ti_{23.14}Na_{1.45}K_{1.12}Al_{5.07}Si_{101.47}O_{258.11}$	29.29	Anatase	8.77	6.2	20.02	116.3	2.72	3.33
ACP3	$Ti_{23.85}Na_{1.44}K_{0.27}Al_{3.31}Si_{138.35}O_{130.22}$	30.20	Anatase	9.25	10.4	41.79	50.1	2.81	3.32
ACP4	$Ti_{24.49}Na_{1.59}K_{0.61}Al_{4.80}Si_{132.93}O_{330.22}$	31.01	Anatase	10.01	14.5	27.68	51.3	2.91	3.43
ACP5	$Ti_{24.29}Na_{1.47}K_{0.35}Al_{2.86}Si_{108.83}O_{271.44}$	30.76	Anatase	14.92	19.0	38.11	44.8	2.85	3.22
ACP6	$Ti_{33.93}Na_{1.64}K_{0.21}Al_{2.79}Si_{129.96}O_{332.96}$	42.95	Anatase	17.36	16.0	46.48	43.6	2.80	3.28
ACP7	$Ti_{36.87}Na_{1.57}Al_{1.52}Si_{137.46}O_{351.80}$	46.68	Anatase	17.72	20.0	90.62	35.6	2.50	3.57

[a] Determined from ICP data. [b] Determined from XRD patterns according to Schererr's equation. [c] Determined from SEM images. [d] Determined from ICP data. [e] BET surface area determined from N_2 adsorption–desorption isotherms.

XRD patterns of ACP2, ACP5 and ACP7 displayed similar observations as shown in Fig. S2A of the ESI† section.

The SEM images of natural CP, TiO_2 and TiO_2/CPs (ACP1, ACP3, ACP4, and ACP6) are illustrated in Fig. 2. As can be seen, the pure natural CP (Fig. 2a) revealed smooth sheet-like structures, while that of TiO_2/CPs (Fig. 2 from b to e) presented rough surfaces with nanoscale particles of TiO_2 with a size of around 4.7–20.0 nm determined from ImageJ software[27] (as shown in Table 1), which were dispersed on the surface of the CP support.

Fig. 2 SEM images of (a) natural CP, (b) ACP1, (c) ACP3, (d) ACP4, (e) ACP6, and (f) pure TiO_2.

These nano-scale TiO_2 particles loaded onto CP support are beneficial to provide more active sites for synergistic effects in the photocatalytic degradation of CV and MO dyes. As can be seen in Fig. 2b and c, both ACP1 and ACP3 prepared in the absence of F^- ions maintained the sheet-like structure of the CP support. However, Fig. 2d and e indicated that the TiO_2 loadings in ACP4 and ACP6 were relatively uniform but there were no apparent sites of unloaded CP. Thermal shocks at high hydrothermal temperature (200 °C) and the existence of F^- ions would cause the excessive dealumination and etching phenomena of the CP supports in ACP3-ACP7, leading to the partial dissolution of the CP framework and good dispersions of the loaded TiO_2, similar to the XRD results. The SEM image of bare TiO_2 (Fig. 2f) exhibited obvious aggregation and therefore indicated that CP supports could act as dispersants to avoid the typical tendency of TiO_2 to form agglomerates.

The SEM images of ACP2, ACP5 and ACP7 as shown in Fig. S3 of the ESI† section exhibited almost similar information to that of ACP1, ACP4 and pure TiO_2, respectively. The use of relatively high concentrations of F^- ions (up to 0.35 M) easily led to the severe aggregation of loaded TiO_2 as seen in ACP7 (Fig. S3c†), which looks like pure TiO_2 (Fig. 2f).

The micro/nanostructures of the ACP3 and ACP6 were further characterized by TEM images. As manifested in Fig. 3a and b, the grain micro-photos of ACP3 and ACP6 were composed of a large amount of TiO_2 nanocrystals with an average size of about 3 and 2.7 μm, respectively. The high magnification TEM image of ACP6 exhibited relatively large and highly crystalline TiO_2 particles with more uniform and independent distributions on the surface of the CP support (Fig. 3d), which is very useful for improving its photocatalytic properties, as compared to that of ACP3 (Fig. 3c), in which the severe aggregation of loaded TiO_2 appeared. The mean sizes of the loaded TiO_2 nano-particles in ACP3 and ACP6 determined from high magnification TEM image using ImageJ software[11,28] were found to be around 10.4 nm (Fig. 3c (inset)) and 19 nm (Fig. 3d (inset)), respectively, consistent with that calculated from SEM images (as shown in Fig. 2c and e) and XRD patterns (as shown
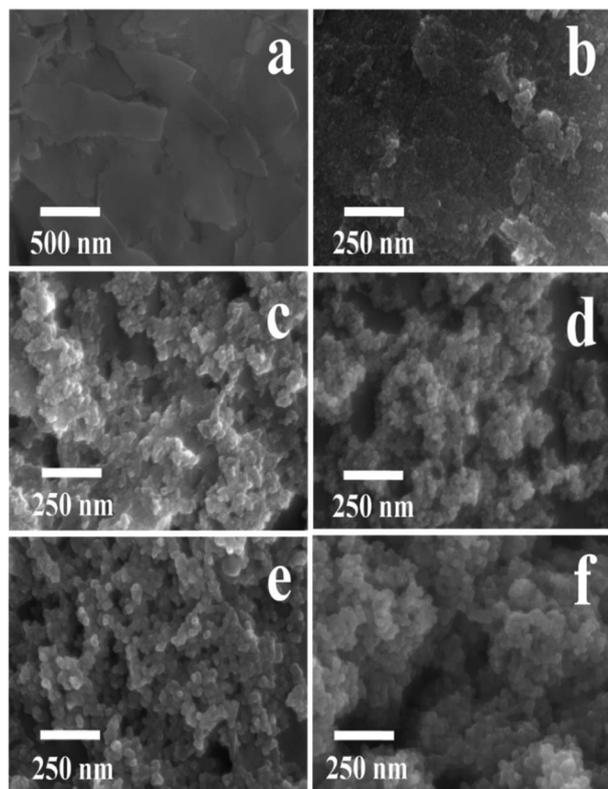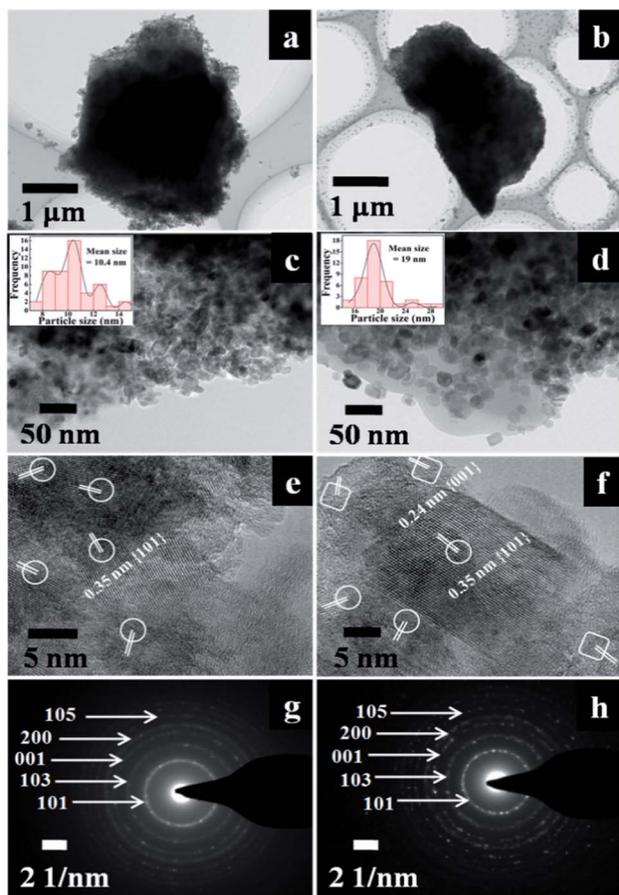
Fig. 3 (a) and (b) TEM images of ACP3 and APC6, (c) and (d) high-magnification TEM images of ACP3 and APC6, (e) and (f) high-resolution TEM images of ACP3 and APC6, (the selected areas in elliptical shapes represent {101} facets, while those in box shapes represent {001} facets) and (g) and (h) the SAED pattern of ACP3 and APC6. The histograms of TiO_2 particle size distribution determined from the high-magnification TEM images of ACP3 and ACP6 are given in the inset of (c) and (d).

in Fig. 1c and e). The high-resolution TEM image of ACP3, as shown in Fig. 3e, revealed that the lattice spaces of 0.35 nm supporting the exposed facets are {101} of the anatase TiO_2. The high-resolution TEM image of ACP6 (Fig. 3f) presented a clear lattice with well-defined lattice fringes of 0.24 and 0.35 nm, corresponding to {001} and {101} exposed facets, respectively, which confirmed the anatase phase of TiO_2.[9] These observations further proved that the existence of F^- ions could be beneficial for the etching effect and formation of the co-exposed {001} and {101} facets of TiO_2 in TiO_2/CPs.[9]

The different crystallographic exposed facets of TiO_2 nanocrystals are controlled by altering their relative stability during the crystal growth, which is intrinsically determined by their surface energies. The capping agents (F^- ions) adsorbed on the surface of TiO_2 interact differently with different crystalline facets leading to various dominant reactive facets.[29] The capping agents (F^- ions) play a crucial role of selectively adsorbing on the surface of TiO_2 and reducing the surface free energy with more active {001} facets of loaded TiO_2, which

results in preserving the highly reactive facets. The selected areas in the elliptical shape represent {101} facets, while that in the box shape represents the {001} facets. According to Wolff's construction principle,[9] more than 90% of the exposed facets consist of the thermodynamically stable {101} facet during the crystal growth process of TiO_2. The co-existence of the reactive high energy {001} facet (0.90 J m^{-2}) and the thermodynamically stable {101} facet (0.44 J m^{-2}) may be beneficial to produce a number of thermal intermediate interfaces with a reduction of their Gibbs free energy,[30] and thereby enhance the synergistic removal of CV and MO dyes from aqueous solution.

The corresponding SAED patterns of ACP3 and ACP6, as shown in Fig. 3g and h, respectively, further demonstrated the existence of the anatase phase of loaded TiO_2. The SAED pattern of ACP6 (Fig. 3h) exhibited more bright circular fields, indicating its high crystalline characteristics, as compared to that of ACP3 (Fig. 3g).

Fig. 4A illustrates the FT-IR spectra of parent CP and TiO_2/CPs (ACP3 and ACP6) in the wavenumber range of 400–4000 cm^{-1}. As can be seen, all samples exhibited almost the same peak profiles, suggesting that the synthesis method did not cause significant destruction of the HEU microstructure. However, the intensity of all peaks in TiO_2/CPs related to CP support became weak, consistent with that of XRD analysis. The most intense peak at around 1030 cm^{-1} was associated with the asymmetric stretching vibration of O–Si(Al)–O, showing high sensitivity to the degree of dealumination.[31] This band became
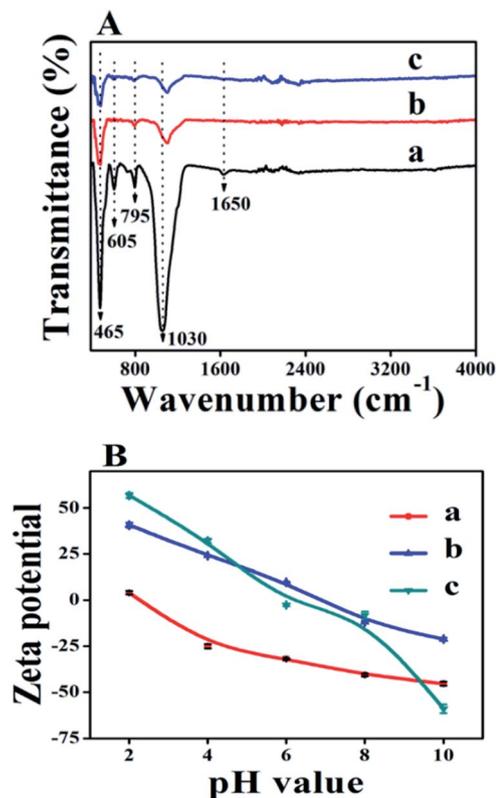

Fig. 4 (A) FT-IR spectra of (a) CP, (b) ACP3, (c) ACP6. (B) Zeta potential of (a) CP, (b) ACP6, and (c) TiO_2.

weak and shifted to a relatively higher wavenumber (1100 cm^{-1}) in TiO$_2$/CPs (Fig. 4A-b and c), as compared to that of parent CP (as shown in Fig. 4A-a). This decrease in intensity and the slight shift in the position of the absorption band around 1030 cm^{-1} may be due to the elution of a portion of the Al^{3+}/Si^{4+} intra-framework on hydrothermal treatment.[32] The peaks that appeared at around 465, 605, and 795 cm^{-1} were attributed to the stretching vibrations of SiO$_4$ and AlO$_4$ tetrahedral atoms present in the zeolite structure.[33] The absorption band at around 1640 cm^{-1} in CP (Fig. 4A-a) was assigned to the –OH bending vibration of physically adsorbed water. This band became very weak in TiO$_2$/CPs, which was due to the desorption of physically adsorbed water during hydrothermal treatment. The intensity of all peaks below 1000 cm^{-1} belonging to CP features decreased after loading TiO$_2$ in the HEU structures, which may be due to the overlapping of the Si–O–Si band of CP and Ti–O band of TiO$_2$.[34] However, the existence of peaks between 400 and 1200 cm^{-1} in all the TiO$_2$/CPs reflected that the skeleton structure of CP was not destroyed after hydro-thermal treatment, thus supporting XRD analysis.

The FT-IR spectra of ACP1, ACP2, ACP4, ACP5 and ACP7 are shown in Fig. S2B of the ESI† section, exhibiting almost the same information as that of ACP3 and ACP6. The absorption bands centered at 430 and 740 cm^{-1} in TiO$_2$ (Fig. S2B-f†) may be attributed to the bending vibration of the Ti–O–Ti bonds.[34]

The zeta potentials of the parent CP, bare TiO$_2$ and TiO$_2$/CP (ACP6) as a function of equilibrium pH of the solution in the range of 2–10 are shown in Fig. 4B. The observed variation in the zeta potentials of all samples with different pH values is due to the acid and base used to adjust the pH values of the media. The zeta potential of bare CP was found to be highly negative in the pH range studied, which is consistent with that reported by Ullah *et al.*[14] The surface charges of TiO$_2$ and ACP6 were found to be positive at low pH value due to the effect of highly acidic TiCl$_4$ aqueous solution during their synthesis. The pH values of point of zero charge (pH$_{pzc}$) for CP (Fig. 4B-a), bare TiO$_2$ (Fig. 4B-c), and ACP6 (Fig. 4B-b) were found to be 2.3, 5.9, and 6.9, respectively.

The surfaces of these samples at a pH value above their pH$_{pzc}$ were negatively charged, whereas they were positively charged at pH below pH$_{pzc}$. Therefore, it was concluded that the surface of bare CP is highly negatively charged, while the hydrothermal treatment of CP under highly acidic TiCl$_4$ aqueous solution leads to a relatively higher value of pH$_{pzc}$, *i.e.* 6.9 of the TiO$_2$/CP.

The XPS spectra of ACP3 and ACP6 are shown in Fig. 5. In Fig. 5A, the XPS spectra of the survey scan exhibited that the peaks of Ti, O, C and Si were common in both ACP3 and ACP6 samples, whereas a weak extra peak of F appeared in the spectrum of ACP6. The two strong peaks at 458.22 and 463.96 eV in the high-resolution XPS spectra of Ti2p (Fig. 5B) correspond to Ti^{4+}2p$_{3/2}$ and Ti^{4+}2p$_{1/2}$, respectively, consistent with the values of Ti^{4+} in the TiO$_2$ lattice. The high-resolution XPS spectra of O1s (Fig. 5C) presented two clear peaks at 529.55 and 532.96 eV, which were assigned to the metal–oxygen bond (lattice oxygen) and oxygen defects sites, respectively.[35] The peak at 532.96 eV representing oxygen vacancy was stronger in ACP6 (Fig. 5C-b) as compared to ACP3 (Fig. 5C-a), indicating the significant role of
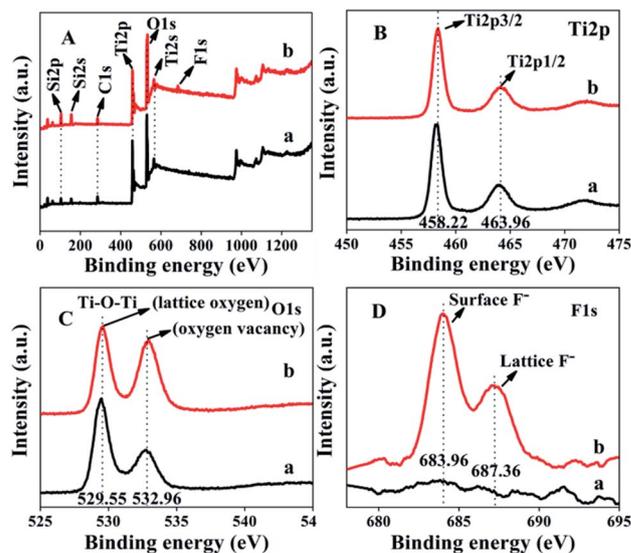

Fig. 5   XPS spectra of the survey scan (A), Ti2p (B), O1s (C) and F1s (D). (a) ACP3 and (b) ACP6.

F$^-$ ions in creating oxygen vacancies. Additionally, the C1s peak (Fig. 5A) arises from the adventitious hydrocarbon present in the high vacuum of the XPS instrument. The ACP6 sample (Fig. 5D-b) clearly revealed two distinct peaks at 683.96 and 687.36 eV, which correspond to the F1s level, whereas ACP3 (Fig. 5D-a) contained no such peaks. The F1s binding energy of 684 eV in Fig. 5D-b corresponds to F$^-$ adsorbed on TiO$_2$ in ACP6, whereas the binding energy of 687 eV showed signs of F ions in the lattice of TiO$_2$ in ACP6.[36]

UV-vis absorption spectra of the TiO$_2$/CPs were obtained to estimate the optical bandgaps, which were determined using the Tauc relation given in eqn (3).

$$(Ah\nu)^n = C(h\nu - E_g) \tag{3}$$

where A is the absorbance, h is Planck's constant, ν is the frequency and E_g is the bandgap energy. The integral n has values of 2 and 1/2 for the allowed direct and allowed indirect transitions, respectively. The optical band gaps were determined by extrapolating the linear portion of the $(Ah\nu)^n$ *vs.* $h\nu$ plot to the y-axis = 0, which gives the bandgap energy (E_g). The obtained optical band gap energy values of the TiO$_2$/CPs, as listed in Table 1, indicate their semiconducting properties.

The chemical formulas of TiO$_2$/CPs and the TiO$_2$-loaded amount determined from ICP are summarized in Table 1. The increased Si/Al ratios along with the enhancement of the hydrothermal treatment temperature and concentrations of used F$^-$ ions are due to the excessive dealumination of the CP supports. As can be seen, although the prepared TiO$_2$/CPs had a higher surface area than the bare CP, their BET surface areas decreased gradually as the particle size of TiO$_2$ loaded on the surface of CPs increased from 7.8 to 17.7 nm.

Pure CP has a relatively low BET surface area of around 15.8 m^2 g^{-1}. The BET surface area was first increased in TiO$_2$/CPs formed at a relatively low hydrothermal temperature, *i.e.* ACP1

and ACP2 with 193.7 and 116.3 $m^2\,g^{-1}$, due to the relatively low particle size of loaded TiO_2 (around 4.7 and 6.2 nm) in these samples. As the particle size of loaded TiO_2 increased, the BET surface area decreased abruptly due to the fact that surface area and particle size were inversely related.

The pore size distribution curves of pure CP and TiO_2/CPs are shown in Fig. S4 of the ESI† section. Pure CP bears pores of both micro- (pore size < 2 nm) and meso-dimensions (pore size > 2 nm), while all of TiO_2/CPs were mesoporous in nature. This is due to the fact that the micropores of CP are filled by the small loaded-TiO_2 nanoparticles. The broadly distributed mesopores in TiO_2/CPs are due to aggregations of intra-particles during the hydrothermal procedures.

3.2. Photodegradation performances

To demonstrate the application of fabricated samples, their photocatalytic activities for the synergistic removal of CV or MO dyes from aqueous solutions were investigated under UV-irradiation. Prior to photocatalytic degradation, the dye solutions containing photocatalysts were stirred continuously for 30 minutes in the dark to reach the adsorption–desorption equilibrium. The amount of each dye adsorbed was found to be less than 5% for all the synthesized TiO_2/CPs. However, it was observed that bare CP exhibited good adsorption properties for CV dye, with 51% removal, while there was poor adsorption with 2% removal for the MO dye. The effect of UV-light on the photodegradation behavior of CV and MO dyes was investigated by carrying out a blank experiment under UV-irradiation in the absence of photocatalyst. Only about 5% degradation of each dye was obtained under UV-irradiation within 180 minutes. The efficiency of the photocatalytic reaction was affected by the characteristic properties of the synthesized TiO_2/CPs, such as crystal structure, particle size, surface charge, surface area, and reaction conditions like the pH of the solution, dose of catalyst, and concentration of pollutant, *etc.* Therefore, to elucidate the effect of operational parameters on the photodegradation performance, the reaction conditions were kept constant. The influences of various parameters on the photocatalytic activity of CV and MO dyes are thoroughly investigated and given in the following results and discussion section.

3.2.1. The effect of the type of catalyst. Prior to photocatalytic degradation, the adsorption–desorption equilibrium was satisfied under continuous stirring for 30 minutes in the dark. Using TiO_2/CPs as the photocatalyst, their photocatalytic activities in the degradation of CV and MO dyes were assessed.

The photocatalytic activities of ACP1, ACP3, ACP4, ACP6 and pure TiO_2 are shown in Fig. 6, while those of ACP2, ACP5 and ACP7 are shown in Fig. S5 of the ESI† section. As can be seen, the degradation efficiencies were higher using TiO_2/CPs as photocatalysts, as compared with the photolysis alone and bare CP (as shown in Fig. S6†). The photocatalytic activity increased as the hydrothermal temperature increased, in the following order: ACP1 < ACP2 < ACP3, or ACP4 < ACP5 < ACP7 < ACP6 when the concentration of F^- ions (as shown in Fig. 6 and S5†) was enhanced, which was also evidenced by the values of the pseudo-first-order rate constants calculated for these catalysts
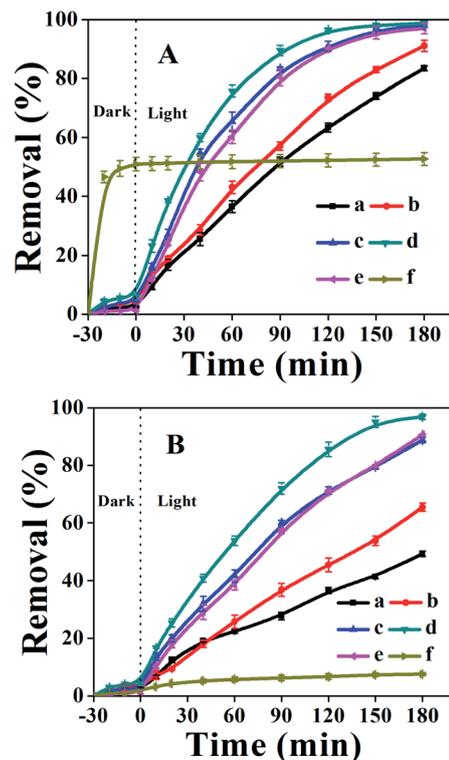

Fig. 6 The effects of various catalysts on the adsorption equilibrium and photocatalytic degradation of CV (A) and MO (B) dyes: (a) ACP1, (b) ACP3, (c) ACP4, (d) ACP6, (e) pure TiO_2, and (f) pure CP. Conditions: initial concentration of dye = 0.0245 mM, catalyst dose = 0.5 g L^{-1}, pH = 6.0, room temperature.

(as shown in Table S2 of the ESI† section). The possible explanation for the marked differences in their photocatalytic behaviors is related to the particle size of the loaded-TiO_2 and their exposed crystal facets. In detail, the ACP1, ACP2, and ACP3 exhibited relatively low photocatalytic activities, which may be due to the smaller particle size of loaded TiO_2 (as shown in Table 1, calculated from XRD patterns and SEM images). Furthermore, the high-resolution TEM image of ACP3 (Fig. 3e) depicted that the exposed surfaces were dominated by the thermodynamically stable low energy {101} facet, which also accounts for their low photocatalytic activity. ACP4–ACP6 showed a linear increase in photocatalytic activity with the increase in the particle size of loaded TiO_2 (as shown in Table 1). Although ACP7 had a high particle size of loaded-TiO_2, as compared to ACP6, it exhibited relatively low photocatalytic activity, mainly due to the severe aggregation of loaded TiO_2, as seen in SEM images (Fig. S3c†). ACP6 showed the best photocatalytic performance among all the synthesized photocatalysts with 98.7 and 96.8% degradation of CV and MO dyes, respectively. The probable reasons for the best photocatalytic performance of ACP6 are due to the more uniform distributions, suitable size of the loaded-TiO_2 particles, and particularly the dominant reactive {001} exposed facet of the nanocrystals, which effectively enhanced the charge separation of the photocatalyst. Moreover, the relatively high number of oxygen vacancies in ACP6 produced by the use of F^- ions, as

demonstrated in XPS results (Fig. 5C-b), is another important factor for its enhanced photocatalytic performance. Therefore, ACP6 was selected as the optimum photocatalyst for further exploration.

3.2.2. The effects of the dose of the catalyst and the initial pH of solution. Different doses of ACP6, *i.e.* 0.15, 0.25, 0.5, 0.75, 1.00, and 1.25 g L^{-1}, were used to determine the optimum amount of photocatalyst for the degradation of CV and MO dyes. Before the irradiation experiments, the suspensions were shaken for 30 min in dark conditions to reach the adsorption–desorption equilibrium. As can be seen in Fig. 7A, the degradation rates of CV (Fig. 7A-a) and MO (Fig. 7A-b) dyes firstly increased to 80.0 and 71.7%, respectively, with increasing the dose up to 0.75 g L^{-1}, and then decreased to 73.5 and 66.7% for CV and MO dyes, using a dose of 1.25 g L^{-1}. Their relatively low degradation rates with lower doses, *i.e.* 0.15, 0.25, and 0.5 g L^{-1}, were because fewer catalyst particles interacted with UV light to produce the reactive radicals, *i.e.* $^{\cdot}OH$, $O_2^{\cdot-}$ *etc.*[37] The decrease in degradation using larger doses, *i.e.* 1.00, and 1.25 g L^{-1}, might be due to the scattering effect of the excess particles, which masks some parts of the photosensitive surface, making it difficult for UV-light to pass through the solution. Hence, the penetration depth of photons decreases and fewer catalyst particles can be activated. Aggregation of the catalyst particles at larger doses also reduces the effective surface area of the used catalyst,[38] which in turn reduces the degradation efficiency.

Fig. 7 The effects of the dose of ACP6 catalyst (A) and the initial pH of the solution (B) on the photocatalytic degradation of CV (a) and MO dyes (b). Conditions: initial concentration of dye = 0.0245 mM, time = 60 min, pH in dose study = 6.0, or catalyst dose in pH study = 0.75 g L^{-1}, and room temperature.

Based on the best degradation properties, the dosage of 0.75 g L^{-1} was selected as the optimum amount and therefore all other investigations were performed with this dose.

The pH of the reaction medium is also an important factor due to its strong influences on the charge of the catalyst.[39] While keeping other conditions constant, the effect of the pH value on the photocatalytic degradation of CV and MO dyes was investigated. As shown in Fig. 7B, the degradation efficiency of both dyes first increased by raising the solution pH from 2 to 8 and thereafter decreased. In detail, the photocatalytic degradation was around 57 and 48% for CV and MO, respectively, at a low pH value of around 2.0, but gradually increased to 85 and 79% for CV and MO with increasing the initial pH (up to 8) of the solution. As shown in Fig. 7B-b, the pH_{pzc} value of 6.9 determined for ACP6 had a direct influence on the photocatalytic degradation of dyes. The ACP6 surface at $pH < pH_{pzc}$ is positively charged, which hinders the adsorption of cationic CV and MO dyes, leading to the low degradation rate.[40] Furthermore, at $pH < pH_{pzc}$, there is competition between the cationic dyes and H^+ ions for the adsorption sites of ACP6; therefore, small amounts of CV and MO dyes with relatively low positive charges were adsorbed on the surface of the ACP6, consequently reducing the degradation efficiency.

Both dyes presented the highest degradation efficiency at pH of 8 and then a small decrease in degradation efficiency occurred at pH 10. These results are similar to those reported by Liu *et al.*[41] The decreased degradation efficiency at $pH > 8$ should be due to the appearance of repulsive forces between the highly negatively charged surface of ACP6 and free electron pairs of the CV and MO dyes. Therefore, relatively fewer molecules of dyes can reach the ACP6 surface where the highly reactive $^{\cdot}OH$ radicals are generated. Furthermore, two types of reactions might occur, such as (i) the reaction of $^{\cdot}OH$ with $^{\cdot}OH$ due to the presence of greater amount of $^{\cdot}OH$ radicals;[41] (ii) the reaction of $^{\cdot}OH$ with ^-OH, at high pH values producing relatively less reactive species,[42] and consequently reducing the percentage degradation.

3.2.3. The effect of irradiation time. The effect of UV-irradiation time on the degradation of CV and MO dyes is shown in Fig. S7A.† The degradation rate of both dyes increased gradually by increasing irradiation time. At the irradiation time of 120 min, the degradation percentages of CV and MO dyes were 98.7 and 97.0%, respectively. The UV-visible absorption spectra of CV and MO dyes after different intervals of photocatalytic degradation are illustrated in Fig. S7B and C,† respectively. The diminishing intensity of the peaks at 582 and 465 nm for CV and MO dyes, respectively, revealed their removal by photocatalytic degradation.

The extent of mineralization of dyes can be also determined by its TOC removal efficiency analysis because complete decolorization does not mean the complete mineralization of the dye. However, on using ACP6 as a catalyst, the relatively low TOC removal (81.1%) of the CV dye after 180 minutes as compared to the decolorization percentage (98.7%) indicated that the complete mineralization of CV dye needed a longer time. Similarly, the TOC removal percentage (78.4%) of MO dye after 180 minutes was also lower than that its decolorization
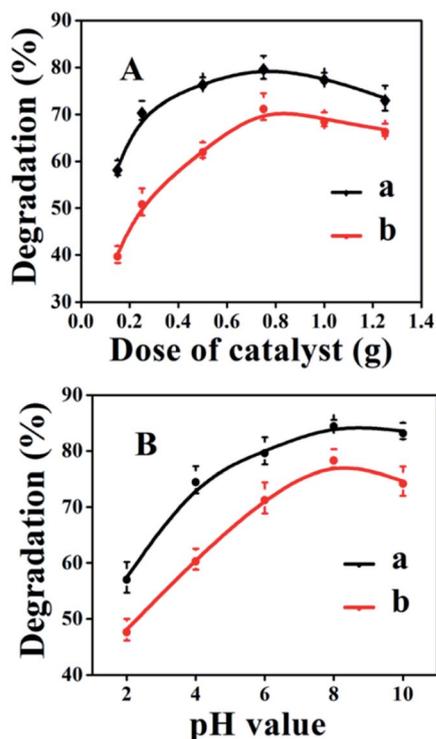
percentage (96.8%). The rapid decrease in the colour removal of the dye might be due to the cleavage of the chromophores, while the low percentage of TOC removal might be due to the formation of intermediates due to the presence of N atoms in both CV and MO dyes.[43]

3.2.4. The effects of initial dye concentration. In order to investigate the effects of the initial concentration of CV and MO dyes on the photocatalytic degradation performance, four different concentrations, *i.e.* 0.0122, 0.0245, 0.0368, and (d) 0.0490 mM of the dyes were used, as shown in Fig. 8. The results showed that the initial concentrations of both the dyes had an obvious influence on the photocatalytic degradation rate. The lower the initial concentration, the faster the degradation rate and *vice versa*. In detail, the percentage degradation was found to be 93.6 and 76.1% for CV and MO, respectively, at low concentration (0.0122 mM), but reduced to 50.9 and 34.5% at higher concentration (0.0490 mM), which may be because the different initial concentrations of the dyes were made to react with a fixed number of ˙OH radicals produced from a given amount of photocatalyst and UV-light. Furthermore, the reactive solution became more opaque with increasing the initial concentration of the dyes, and penetration of UV-light through the solution to reach the catalyst surface became more difficult; consequently, relatively fewer highly reactive ˙OH radicals were produced.

The kinetic behavior of heterogeneous photocatalytic reactions is generally described by the Langmuir Hinshelwood equation, which states that the initial degradation rate (r) of organic compounds is proportional to the surface coverage (θ),[44] as follows:

$$r = -\mathrm{d}c/\mathrm{d}t = k\theta = k(KC/1 + KC) \tag{4}$$

where r is the rate of reaction, k is the rate constant, K is the Langmuir constant, C is the initial concentration of the dye solution (mM), and c is the concentration of dye at time t (min). For concentrated solutions where $C > 5.0$ mM, then $KC \gg 1$, and the reaction becomes zero order. For dilute solutions where $C < 1.0$ mM, $KC \ll 1$, and the reaction becomes pseudo-first-order. Hence, the diluted solutions of CV and MO were used for photocatalytic degradation experiments. Their kinetics were found to fit the pseudo-first-order kinetic rate expression (5):

$$\ln C_0/C = k_{\mathrm{app}} \cdot t \tag{5}$$

where C_0 and C are the concentrations (ppm) of the dyes at times 0 and t (min), respectively, k_{app} is the apparent rate constant and t is the time interval. A linear correlation was observed between $\ln(C_0/C)$ *vs.* irradiation time using different initial concentrations of dyes, as shown in Fig. 8C and D. A decrease in k_{app} was observed with the increasing C_0 values of both dyes (seen in Table S3†), suggesting a low degradation rate for a high initial concentration of the dyes.

3.2.5. Degradation pathways of CV and MO dyes. The role of active species in the photocatalytic degradation of CV and MO dyes was determined by adding 0.0926 mM of benzoquinone and 0.1667 mM of isopropyl alcohol as scavengers for $O_2^{\bullet-}$
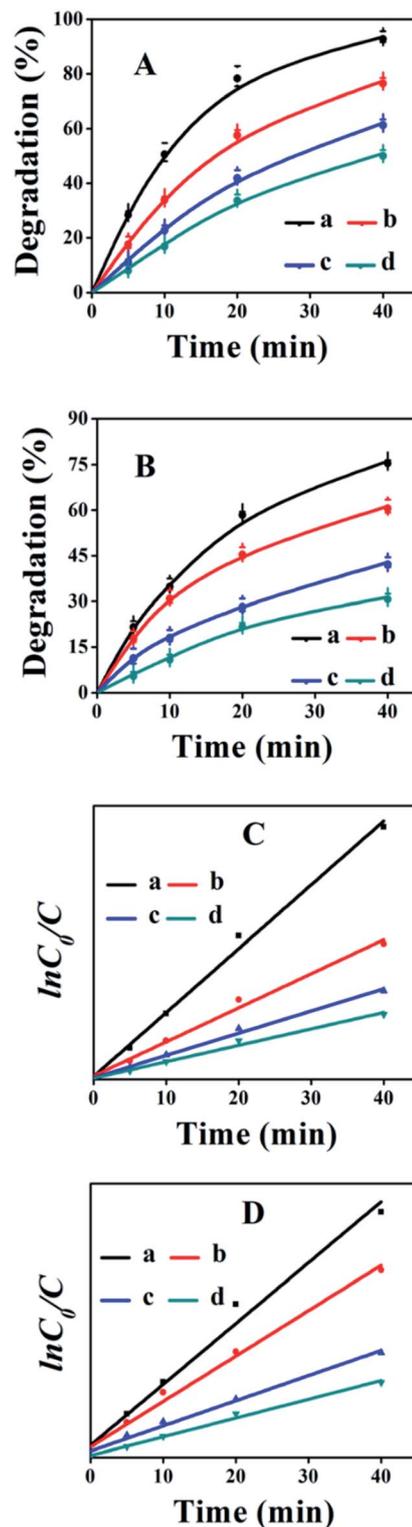

Fig. 8 The effects of initial concentration on the photocatalytic degradation of the CV dye (A) and its corresponding kinetic behavior (C), as well as MO dye (B) and its corresponding kinetic behavior (D). (a) 0.0122, (b) 0.0245, (c) 0.0368, and (d) 0.0490 mM. Conditions: catalyst dose = 1.0 g L^{-1}, pH = 10, room temperature.

and $^{\cdot}OH$ radicals, respectively. Fig. S8† showed the variation in the degradation of CV and MO dyes as a function of irradiation time before and after scavengers were added to the photocatalytic system. As can be seen in Fig. S8,† using ACP6 as the catalyst, the degradation efficiency of CV was reduced from 96 to 27% in the presence of benzoquinine, and reduced to 71% in the presence of isopropyl alcohol. Similarly, the degradation efficiency of MO dye decreased from 79 to 25% in the presence of benzoquinone and to 56% in the presence of isopropyl alcohol. Thus, it can be concluded that the photocatalytic degradation efficiency mainly depends upon the $^{\cdot}OH$ radicals.

The photocatalytic degradation process is initiated by the generation of $^{\cdot}HO$ and $O_2^{\cdot-}$ radicals. When the reaction mixture is illuminated by UV-visible irradiation, the electrons in the conduction band become excited and shift to the valance band. Thus, created holes in the valance band react with water molecules and form $^{\cdot}HO$ radicals, while the electrons from the conduction band react with absorbed oxygen and generate $O_2^{\cdot-}$ radicals.[45] These generated reactive species ($^{\cdot}HO$ and $O_2^{\cdot-}$) are responsible for the degradation of CV dye. According to the literature,[46] the degradation of CV dye mainly follows two processes, as shown in Fig. S9a,† namely (i) the demethylation pathway, and (ii) chromophore cleavage. The CV molecule undergoes demethylation and chromophores cleavage and forms DLPM (bis(4-(dimethylamino)phenyl)methanone), the main intermediate product of CV dye degradation, due to the destruction of the p–π conjugate structure of CV.[46] The dihydroxylation of DLPM generates aromatic compounds, such as benzoic acid, 3,6 dimethyl benzoic acid, and hydroxybenzoic acid, which undergo a ring-opening reaction and generate aliphatic compounds such as ethylene glycol, carbonic acid, and oxalic acid. The final degradation products (CO_2 and H_2O) were formed via the mineralization of aliphatic compounds.

According to the literature,[47,48] the proposed degradation pathway of MO dye is shown in Fig. S9b.† MO dye degradation is initiated with the attack of reactive species on the chromophore (–N=N–), and the cleavage of aromatic rings occurs. The aromatic rings undergo ring-opening reaction and form aliphatic small compounds that further mineralize into CO_2, H_2O, SO_3^- and NO_3^-.

3.2.6. Catalyst recycling. Photocatalyst recycling for reuse is an important factor that can evaluate its stability and economy for practical applications. The recycling studies in this work were carried out using ACP6 as a selective photocatalyst for the degradation of CV and MO over five successive cycles. At the end of each cycle, the catalyst was centrifuged, washed thoroughly with deionized water, acetone and ethanol, respectively, and reused in the next cycle. As shown in Table 2, the decreases in photocatalytic degradation rates of the CV and MO were observed with the repeated use of the catalyst, which were found to decrease from 96% for CV and 93% for MO in the first cycle to 78% and 76% in the fifth cycle, respectively. One of the main reasons for activity reduction may be the adsorption of reaction products on the surface of the catalyst, leading to the blockage of active sites; besides that, the loss of some active sites during the recycling caused a decrease in the degradation rate of the dye. Kanakaraju et al.[10] also observed a decrease in the photocatalytic activity for the degradation of amoxicillin due to the blockage of pores on the surface of the catalyst by the pollutant and its degradation byproducts. In order to generate the activity of the catalyst, they calcined the recovered catalyst. Ullah et al.[14] also observed a reduction in the activity of the TiO_2/clinoptilolite catalyst after repetitive usage. Because the calcination procedure has a great influence on the properties of the loaded-TiO_2 particles, all fresh catalysts in the present study were not calcined during the synthesis process.

4. Conclusions

The effects of the hydrothermal treatment temperature and concentration of F^- ions on the structure, morphology, particle size, exposed crystal facets and photocatalytic activity of TiO_2-supported clinoptilolite (TiO_2/CP) were assessed. The various characterizations of obtained TiO_2/CPs demonstrated that increasing temperature and concentration of F^- ions caused a net decrease in their surface areas and an increase in the particle size of the loaded TiO_2 along with their enhanced crystallinity degree. The presence of F^- ions plays an important role in hydrothermal etching and exposing highly energetic {001} facets of the supported TiO_2. The photocatalytic activity of TiO_2/CPs was evaluated for the synergistic removal of CV and MO dyes under UV-irradiation in aqueous media. The high degree of crystallinity, exposed highly energetic {001} facets, uniform and fine dispersion of TiO_2 in TiO_2/CP (ACP6) caused by the use of F^- ions reflected the higher surface density of the active sites and the separation efficiency of electron–hole pairs, which account for its best photocatalytic performance. Mutually independent exposed {001} and {101} facets of TiO_2 loaded onto the CP supports provide new insight into the design and fabrication of advanced photocatalytic materials.

Author contributions

Anadil Gul and Raza Ullah: equal contribution, investigation, writing original draft preparation; Tallat Munir: data curation; Jihong Sun: supervision, conceptualization, methodology; Shiyang Bai: formal analysis, validation.

Conflicts of interest

There are no conflicts to declare.

Table 2 ACP6 reusability over five successive cycles in the degradation of CV and MO. Conditions: dose of catalyst = 0.75 g L^{-1}, pH = 8, room temperature, time = 90 min, initial dye concentration = 10 ppm

Dye	% Degradation				
	1st cycle	2nd cycle	3rd cycle	4th cycle	5th cycle
CV	96	92	85	81	78
MO	93	90	84	79	76

Acknowledgements

References

1 L. Soares and A. Alves, *Mater. Lett.*, 2018, **211**, 339–342.

2 Q. Wu, H. Yang, H. Zhu and Z. Gao, *Optik*, 2019, **179**, 195–206.

3 B. Paul, W. N. Martens and R. L. Frost, *Appl. Clay Sci.*, 2012, **57**, 49–54.

4 J. Hu, Y. Cao, K. Wang and D. Jia, *RSC Adv.*, 2017, **7**, 11827–11833.

5 X. Liu, Y. Liu, S. Lu, W. Guo and B. Xi, *Chem. Eng. J.*, 2018, **350**, 131–147.

6 O. O. Prieto-Mahaney, N. Murakami, R. Abe and B. Ohtani, *Chem. Lett.*, 2009, **38**, 238–239.

7 H. Cheng, J. Wang, Y. Zhao and X. Han, *RSC Adv.*, 2014, **4**, 47031–47038.

8 K. Tanaka, M. F. Capule and T. Hisanaga, *Chem. Phys. Lett.*, 1991, **187**, 73–76.

9 H. Liu, S. Liu, Z. Zhang, X. Dong and T. Liu, *Sci. Rep.*, 2016, **6**, 33839.

10 D. Kanakaraju, J. Kockler, C. A. Motti, B. D. Glass and M. Oelgemoller, *Appl. Catal., B*, 2015, **166**, 45–55.

11 Z. Mehrabadi and H. Faghihian, *Spectrochim. Acta, Part A*, 2018, **204**, 248–259.

12 M. Khatamian, S. Hashemian and S. Sabaee, *Mater. Sci. Semicond. Process.*, 2010, **13**, 156–161.

13 R. Mohamed, A. Ismail, I. Othman and I. Ibrahim, *J. Mol. Catal. A: Chem.*, 2005, **238**, 151–157.

14 R. Ullah, C. Liu, H. Panezai, A. Gul, J. Sun and X. Wu, *Arabian J. Chem.*, 2020, **13**, 4092–4101.

15 A. H. Mamaghani, F. Haghighat and C. S. Lee, *J. Photochem. Photobiol., A*, 2019, **378**, 156–170.

16 B. G. T. Keerthana, T. Solaiyammal, S. Muniyappan and P. Murugakoothan, *Mater. Lett.*, 2018, **220**, 20–23.

17 R. Ullah, J. Sun, A. Gul and S. Bai, *J. Environ. Chem. Eng.*, 2020, **8**, 103852.

18 H. Dzinun, M. H. D. Othman and A. Ismail, *Chemosphere*, 2019, **228**, 241–248.

19 A. Ahmadpour, A. H. Asl and N. Fallah, *Part. Sci. Technol.*, 2018, **36**, 791–798.

20 C. Z. Wen, J. Z. Zhou, H. B. Jiang, Q. H. Hu, S. Z. Qiao and H. G. Yang, *Chem. Commun.*, 2011, **47**, 4400–4402.

21 M. A. Behnajady, N. Modirshahla, M. Shokri, H. Elham and A. Zeininezhad, *J. Environ. Sci. Health, Part A*, 2008, **43**, 460–467.

22 C. B. Almquist and P. Biswas, *J. Catal.*, 2002, **212**, 145–156.

23 X. Han, X. Wang, S. Xie, Q. Kuang, J. Ouyang, Z. Xie and L. Zheng, *RSC Adv.*, 2012, **2**, 3251–3253.

24 H. G. Yang, C. H. Sun, S. Z. Qiao, J. Zou, G. Liu, S. C. Smith, H. M. Cheng and G. Q. Lu, *Nature*, 2008, **453**, 638–641.

25 N. Roy, Y. Sohn and D. Pradhan, *ACS Nano*, 2013, **7**, 2532–2540.

26 R. A. Sene, S. Sharifnia and G. Moradi, *Int. J. Hydrogen Energy*, 2018, **43**, 695–707.

27 C. A. Schneider, W. S. Rasband and K. W. Eliceiri, *Nat. Methods*, 2012, **9**, 671.

28 H. Zabihi-Mobarakeh and A. Nezamzadeh-Ejhieh, *J. Ind. Eng. Chem.*, 2015, **26**, 315–321.

29 W. J. Ong, L. L. Tan, S. P. Chai, S. T. Yong and A. R. Mohamed, *Nanoscale*, 2014, **6**, 1946–2008.

30 T. R. Gordon, M. Cargnello, T. Paik, F. Mangolini, R. T. Weber, P. Fornasiero and C. B. Murray, *J. Am. Chem. Soc.*, 2012, **134**, 6751–6761.

31 M. Trujillo, D. Hirales, M. Rincon, J. Hinojosa, G. Leyva and F. Castillon, *J. Mater. Sci.*, 2013, **48**, 6778–6785.

32 F. Rahmani, M. Haghighi and M. Amini, *J. Ind. Eng. Chem.*, 2015, **31**, 142–155.

33 N. Davari, M. Farhadian, A. R. S. Nazar and M. Homayoonfal, *J. Environ. Chem. Eng.*, 2017, **5**, 5707–5720.

34 S. Bagheri, Z. A. Mohd Hir, A. Termeh Yousefi and S. B. Abd Hamid, *Desalin. Water Treat.*, 2016, **57**, 10859–10865.

35 L. Wu, L. Shi, S. Zhou, J. Zhao, X. Miao and J. Guo, *Energy Technol.*, 2018, **6**, 2350–2357.

36 H. Park and W. Choi, *J. Phys. Chem. B*, 2004, **108**, 4086–4093.

37 A. Nezamzadeh-Ejhieh and H. Zabihi-Mobarakeh, *J. Ind. Eng. Chem.*, 2014, **20**, 1421–1431.

38 A. Nezamzadeh-Ejhieh and Z. Banan, *Desalination*, 2012, **284**, 157–166.

39 A. Nezamzadeh-Ejhieh and M. Amiri, *Powder Technol.*, 2013, **235**, 279–288.

40 A. Nezamzadeh-Ejhieh and A. Shirzadi, *Chemosphere*, 2014, **107**, 136–144.

41 A. L. Liu, K. Wang, W. Chen, F. Gao, Y. S. Cai, X. H. Lin, Y. Z. Chen and X. H. Xia, *Electrochim. Acta*, 2012, **63**, 161–168.

42 A. Nezamzadeh-Ejhieh and S. Moeinirad, *Desalination*, 2011, **273**, 248–257.

43 M. R. Abhilash, G. Akshatha and S. Srikantaswamy, *RSC Adv.*, 2019, **9**, 8557–8568.

44 Z. Shams-Ghahfarokhi and A. Nezamzadeh-Ejhieh, *Mater. Sci. Semicond. Process.*, 2015, **39**, 265–275.

45 Y. Ju, J. Fang, X. Liu, Z. Xu, X. Ren, C. Sun, S. Yang, Q. Ren, Y. Ding and K. Yu, *J. Hazard. Mater.*, 2011, **185**, 1489–1498.

46 N. Couselo, F. S. García Einschlag, R. J. Candal and M. Jobbágy, *J. Phys. Chem. C*, 2008, **112**, 1094–1100.

47 N. Bahrudin and M. Nawi, *J. Water Process Eng.*, 2019, **31**, 100843.

48 S. Xie, P. Huang, J. J. Kruzic, X. Zeng and H. Qian, *Sci. Rep.*, 2016, **6**, 1–10.